Using Lagrangian filtering to remove waves from the ocean surface velocity field

C. Spencer Jones[1,2], Qiyu Xiao[3], Ryan P. Abernathey [2]and K. Shafer Smith[3]

[1]Texas A&M University, College Station, TX
[2]Columbia University, New York, NY
[3]New York University, New York, NY

Key Points:

- We present a recipe for using Lagrangian filtering to filter waves from the ocean surface velocity field
- Removing super-inertial energy using Lagrangian filtering preserves some super-inertial energy in the Eulerian frame
- Preserved velocities are associated with convergent fronts, suggesting Lagrangian filtering retains transport-active nongeostrophic flows

Corresponding author: C Spencer Jones, `spencerjones@tamu.edu`

Abstract

The Surface Water and Ocean Topography (SWOT) satellite will measure altimetry on scales down to about 15km: at these scales, the sea-surface-height signature of inertia-gravity waves, including barotropic tides and internal tides, will be visible. However, tides and inertia-gravity waves have little impact on tracer transport. Recent work has shown that Lagrangian filtering can be used to isolate the inertia-gravity wave part of the flow. This manuscript presents a recipe for removing barotropic motions and inertia-gravity waves from the surface velocities and from the sea surface height, to estimate the non-wave part of the flow in the Agulhas region of a high-resolution ocean model (LLC4320). First, two methods for removing the barotropic component of sea surface height variability are presented. Then Lagrangian filtering, a method that accounts for Doppler shifting of high-frequency motions by the low-frequency velocity field, is applied to both the sea surface height and the ocean surface velocity field. The results of Lagrangian filtering are presented in spectral space. Lagrangian filtering preserves motions that appear super-inertial in the reference frame of the Earth, while other methods do not preserve these motions as effectively. In some locations most of the energy at high frequencies comes from these Doppler shifted balanced motions. We show that the non-wave part of the velocity field that is preserved more effectively by Lagrangian filtering includes convergent motions near regions of frontogenesis.

Plain Language Summary

Scientists often want to divide up the velocity at the surface into two parts: the part of the velocity that transports ocean tracers (like heat, salt and carbon), and the wave-like part of the velocity that is irrelevant for ocean tracer transport. Lagrangian filtering is a recently discovered method for doing this: it accounts for how the ocean velocities change the frequency of some of the signals we measure through Doppler shift. In this paper, we provide a recipe for using Lagrangian filtering to find the non-wave part of the flow, and we compare Lagrangian filtering to alternative methods. Lagrangian filtering seems to do a better job of revealing the part of the ocean surface velocity that transports tracers.

1 Introduction

Near-surface ocean currents are a critical component of the Earth system, mediating the transfer of heat, momentum, and trace gasses between ocean and atmosphere (Cronin et al., 2019; Elipot & Wenegrat, 2021). These currents regulate marine ecosystems by transporting nutrients and phytoplankton laterally within the eutrophic zone (Barton et al., 2010; Resplandy et al., 2011), and they transport marine debris and plastic pollution around the globe (Van Sebille et al., 2020). Observed ocean surface currents are also used to evaluate the accuracy and biases of numerical ocean models. As a result, the oceanographic community requires accurate and detailed knowledge of the state of ocean surface currents.

Satellite-based observations of sea-surface height (SSH), which is directly proportional to surface pressure, can be used to infer surface velocities via geostrophic balance. Modern ocean altimetry products like Archiving, Validation, and Interpretation of Satellite Oceanographic data (AVISO) (Ducet et al., 2000) typically have grid resolution of around 0.25° and an effective resolution of approximately 200 km. At this scale, geostrophic balance holds well, and altimetry-dervived near-surface geostrophic velocities are used in many studies of ocean currents (e.g., Niiler et al., 2003; Abernathey & Marshall, 2013; Mkhinini et al., 2014, and many others). Direct observations from drogued drifters, such as those from the NOAA Global Drifter Program, are an additional source of surface velocity data. While highly accurate, such measurements are relatively sparse, with approximately one drifter in every 5° x 5° box of the ocean (Elipot et al., 2016).

The recently-launched Surface Water and Ocean Topography (SWOT) satellite will provide altimetry at scales down to ∼15km (Morrow et al., 2019). These measurements have the potential to greatly enhance our understanding of ocean surface currents, particularly at smaller scales. However, the SWOT measurements will also pose two distinct challenges for the estimation of velocities. First, the SWOT signal will presumably contain inertia-gravity waves (including internal tides), which have an imprint on both the SSH and the velocity field (Zaron & Rocha, 2018). Second, even if the waves were to be removed somehow, geostrophy becomes increasingly inaccurate at SWOT scales, where in some regions, the Rossby number (Ro $= 1/\tau f$ where τ is the advective timescale of the flow) gets closer to one and the nonlinear terms in the momentum equation become important (Callies et al., 2020).

In order to make progress on this problem, it is helpful to separate the internal tidal signal, as well as other non-tidal IGW components from the total SWOT SSH signal: this is a major focus of the SWOT science team research (Ponte et al., 2017; Lahaye et al., 2019; Klein et al., 2019). Some applications of near-surface velocities, particularly for the study of transport phenomena, benefit from a wave-free velocity field. The waves can indirectly influence tracer transport by modulating the energetics of the eddy field, but they make a minimal direct contribution to transport due to their quasi-linearity (Plumb, 1979; Balwada et al., 2018). Quasi-linear waves may displace tracer contours but don't cause these contours to fold or filament; nonlinear interactions are usually required to create small-scale tracer structures that enable mixing in the vertical. The barotropic tidal signal is already removed from conventional altimetric SSH as part of the data processing (Stammer et al., 2014).

Even after the IGW signal has been filtered from the surface velocities and the SSH, the height field is unlikely to be in simple geostrophic balance with the velocity field. The remaining parts of the flow include higher-order balances such as gradient-wind and semi-geostrophy, but also the complex interactions between frontogenetic convergence and vertical mixing (e.g. turbulent thermal-wind balance) that don't really qualify as either balanced or wave motions. Still, we need language to describe these non-wave, non-geostrophic flows, so in lieu of a widely-accepted term, we refer to them here as "balanced ageostrophic" motions.

Both balanced geostrophic and balanced ageostrophic motions are likely to be important for transporting tracers in the horizontal, but because geostrophic motion is approximately non-divergent, balanced ageostrophic motions are probably the most important flows for transporting tracers from the surface across the base of the mixed layer (Ferrari, 2011; Lévy et al., 2018; Mahadevan et al., 2020; Uchida et al., 2020). Hence it is important not to accidentally remove balanced ageostrophic motions when removing IGWs from the SWOT SSH signal.

The combined challenges of filtering waves and retaining balanced ageostrophic motions mean that exploiting SWOT for inferring near-surface currents is far from trivial. Removing the IGW signal and studying the relationship between SSH and the balanced velocity field is a promising direction for future research. As a step towards estimating the balanced (transport-relevant) surface currents from SWOT data post launch, this paper investigates part 1 of the problem: how to accurately remove the IGW signal from near-surface ocean currents and preserve the transport-relevant part of the flow. We use a global eddy- and IGW-resolving GCM simulation, the MITgcm LLC4320. This simulation provides a realistic truth signal with much of the same complexity as the real ocean, including both IGWs and balanced ageostrophic motions.

Using this model, we compare and evaluate three different filtering methods for removing IGWs and retaining the transport-relevant part of the surface velocity field. In doing so, we provide a recipe for estimating the balanced part of the flow. Each of these three methods has been used to remove or isolate IGWs in previous work, but the novelty of this paper is that we perform a detailed comparison of these methods at the ocean surface. The first method applies a frequency-based filter at a fixed location, the second method applies a frequency-based filter along particle pathways, and the third method applies a frequency-wavenumber filter to a chosen region of the ocean. A perfect separation between balanced motions, including balanced ageostorophic motions (the so-called 'slow manifold') and inertia-gravity waves (the so-called 'fast manifold') is likely to be impossible, because these categories are sometimes fuzzy. But there are significant differences between the three methods that suggest that some of them are more effective than others. Below, we provide some background about each of these methods.

It has long been known that most inertia-gravity waves have frequencies higher than the inertial frequency. One popular way of estimating the amount of energy in IGWs is to use a purely frequency-based method to isolate these motions. Furuichi et al. (2008); Richman et al. (2012) and Mazloff et al. (2020) all take a timeseries at each fixed physical location and apply a high-pass filter that preserves frequencies higher than the inertial frequency, before integrating over all frequencies to estimate the total energy in IGWs. A purely frequency-based method is also sometimes used to remove IGWs from the total velocity field. For example, Qiu et al. (2020) and Nwankwo et al. (2023) use a low-pass filter at each physical location to remove waves from their velocity field. The first filtering method that we evaluate in this paper is purely Eulerian and frequency-based. Using this method, motions are measured at a fixed location on the Earth, with motions at frequencies lower than the inertial frequency labelled as balanced, and motions at frequencies higher that the inertial frequency labelled as wave-like.

Pinkel (2008), Shakespeare and Hogg (2017) and Caspar-Cohen et al. (2022) show that both balanced flows and IGWs are Doppler shifted by the large scale flow field. This means that fixed-location frequency filtering may be inaccurate, particularly in regions with fast background flows. Shakespeare and Hogg (2017) developed a method of filtering that accounts for this effect. Lagrangian particles are seeded in the horizontal flow field and record the velocity along their trajectories, i.e. in a flow-following coordinate system. Temporal (frequency) filtering is applied to the velocities recorded by each particle, after which the velocities are interpolated onto a regular grid. The second filtering method we use in this paper is Lagrangian filtering, based on the updated method by Shakespeare et al. (2021). In this method, motions are measured in flow-following coordinates, with motions at frequencies lower that the inertial frequency labelled as balanced and motions at frequencies higher the inertial frequency are labelled as wave-like.

Torres et al. (2018) argue that instead of using a purely frequency-based method for identifying internal gravity waves, wavenumber information should also be used. Using LLC4320 output for the Kurushio-Extension region, they plot the kinetic energy in frequency-wavenumber space. They find that at any given wavenumber, the energy at frequencies higher than the tenth baroclinic mode tends to fall along discrete beams aligned with the dispersion relation of each of the baroclinic modes. In their figures, the energy at frequencies below this curve tends to be continuously spread in frequency-wavenumber space, suggesting that it is associated with balanced motions. They subsequently estimate the amount of internal gravity wave energy in the model by integrating the energy at frequencies above the tenth baroclinic mode. The third filtering method in this paper labels motions with frequencies lower than the tenth baroclinic mode in frequency-wavenumber space as balanced, and motions with frequencies higher than the tenth baroclinic mode as wave-like.

This paper compares these three filtering methods: fixed-location frequency filtering (here called ω-filtering), Lagrangian filtering, and filtering frequencies higher than the tenth baroclinic mode (here called ω-k filtering). Our goal is to understand the differences between the three methods. We focus on Lagrangian filtering, which has not been substantially tested at the ocean surface.

Our results suggest that, in regions with strong mesoscale surface currents, Lagrangian filtering preserves a significant amount of horizontal flow that appears to be at super-inertial frequencies when measured at a fixed location. ω-filtering does not preserve these motions, and ω-k filtering only preserves some of these motions. We then examine the velocities that are preserved by Lagrangian filtering, to evaluate whether their properties are consistent with balanced flow. We use vorticity-strain joint probability-density functions to assess the effectiveness of each filtering method. Recent results from Balwada et al. (2021) show that fronts occupy a particular region of vorticity-strain space: if the filtered flow retains these features, then it is likely that fronts are being (correctly) categorized as balanced. We also examine the divergence field of the filtered velocities in physical space.

The three methods compared here are not the only possible methods for separating the balanced and wave-like parts of the flow. Other possible methods include linear and non-linear eigenvector methods (Kafiabad & Bartello, 2016; Chouksey et al., 2018; Eden et al., 2019), and methods that assume the potential vorticity is conserved and cannot be transferred to inertia-gravity waves (Viúdez & Dritschel, 2004; Masur & Oliver, 2020; Onuki, 2020). Most of these methods would require us to make significant assumptions about the initial condition, the lateral boundary conditions, the wind and other external forcing. However, they are useful for studying wave-mean interactions in models, and may be adapted to analyze LLC4320 data in the future.

Section 2 describes the region of LLC4320 used in this paper, together with the various methods used to filter the velocity and SSH fields: section 2.1 describes the removal of barotropic signals from the SSH and section 2.2 describes the different filtering methods used in this work. In section 3.1, we plot the frequency spectrum of horizontal velocity and SSH for the three filtering methods. Section 3.2 describes the frequency-wavenumber spectra of horizontal velocity for the three filtering methods. Section 3.3 and section 3.4 examine the properties of the velocities that are labeled as balanced by each filtering method, using joint probability density functions and the divergence combined with the frontogenesis function. A summary of our results and some conclusions are presented in section 4.

2 Methods

This study focuses on 75 days of SSH and velocity data taken from the Agulhas region of the LLC4320 simulation (Rocha et al., 2016), which is a 1/48° global configuration of the MITgcm. The model includes tides, permits submesoscale variability and is able to resolve the IGW field at scales larger than 10km or so (Savage et al., 2017). The large data volume of the LLC4320 model, together with the large computational cost of the Lagrangian filtering method, compelled us to focus on a limited region of the ocean. This region was selected because of the presence of strong mesoscale flow features, including the Agulhas retroflection and the Antarctic Circumpolar Current. The chosen region, which is the same region used in Sinha et al. (2019), is shown in figure 1, and the time period extends from October to December 2011.

We compare several methods of partitioning the surface velocities, as detailed in section 2.2. One of these methods requires the data to be transformed into frequency-wavenumber space. Because of the curvature of the globe and the presence of land in the domain, it is not possible to apply this transformation to the whole domain at once. Hence, we choose to compare filtering methods in two regions of the domain: region A (shown by the blue box in figure 1) and region B (shown by the green box in figure 1). Region A is chosen because it has a lot of energy in the inertia gravity wave field, whereas region B is chosen because it has strong velocities at the mesoscale. Comparing these regions allows us to evaluate the differences between filtering methods in a region where IGWs are strong to one where they are relatively weak.

In both region A and region B, we estimated the Rossby number as a function of scale using $\mathrm{Ro} = [\tau(k)f]^{-1}$ (where $\tau(k) = (k^3\langle|\hat{\mathbf{u}}|\rangle^2/2)^{-1/2}$ and $\langle|\hat{\mathbf{u}}|^2\rangle/2$ is the kinetic energy spectrum; Callies et al. (2020)), and found that the maximum Rossby number occurred at the 10-20km length scale in both regions. In region A, this maximum Rossby number is 0.3 and in region B the maximum Rossby number is 0.5. Of course, higher Rossby numbers may be possible at smaller scales, but processes at scales smaller than 10km are not completely resolved in LLC4320. At the smallest scales expected to be resolved by SWOT, we expect that non-geostrophic motions will be just as important as geostrophic motions in many regions.

2.1 Removing the barotropic signal from the sea surface height

The SSH contains variability that is associated with both balanced motions and with IGWs. It also contains barotropic motions, including the effects of barotropic tides, surface pressure changes and wind forcing. Because these barotropic motions have both subinertial and superinertial frequencies, the filtering methods described in section 2.2 are not designed to remove barotropic variability. Hence, we need to remove the barotropic part of the SSH variability before applying any other filtering method to the SSH field.

The tidal forcing of LLC4320 contains eight short-period tidal components, K_1, O_1, P_1, Q_1, M_2, S_2, N_2, and K_2 (Zhao et al., 2019), but LLC4320 has much more energy in the semidiurnal band than observations (Savage et al., 2017; Yu et al., 2019; Luecke et al., 2020). This is probably caused by the horizontal resolution, which resolves tidal forcing and propagation, but does not resolve the associated dissipative processes (Buijsman et al.,

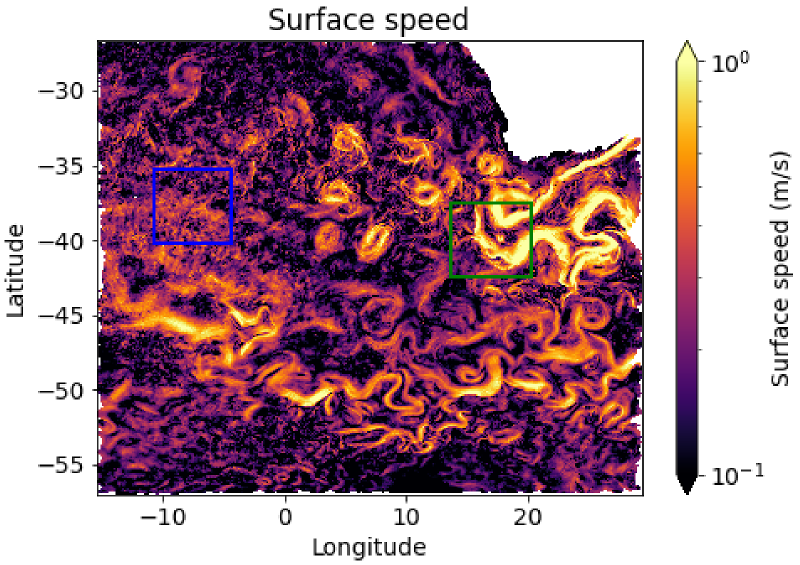

Figure 1. Snapshot of surface speed in our domain. The blue box is region A and the green box is region B. The white area in the north west of the domain is the southern part of Africa. The white areas around the edge indicate locations where seeded particles leave the domain within the 72 hour particle run.

2020). Because of this difference from observations, an off-the-shelf tidal model tuned to the real ocean (e.g. the TPXO model, Egbert et al. (1994); Egbert and Erofeeva (2002)) is unlikely to be suitable for removing the barotropic tide from sea surface height in LLC4320. In any case, we wish to remove all barotropica signals, and not just the barotropic tidal signal.

Another common way to filter out the barotropic signal (including barotropic tides, pressure- and wind-forced barotropic variability) is to use the steric height. The total SSH, η, is

$$\eta(x,y,t) = \underbrace{\frac{p_b'(x,y,t)}{\rho_0 g} - \frac{p_a(x,y,t)}{\rho_0 g}}_{\text{non-steric}} \underbrace{- \int_{-H}^{0} \frac{\rho'(x,y,z,t)}{\rho_0}\, dz}_{\text{steric}}\,, \tag{1}$$

from Wang et al. (2018), where H is the ocean depth, $p_b' = p_b - \rho_0 g H$ represents the bottom pressure anomaly, p_a is the atmospheric pressure, and the density $\rho = \rho_0 + \rho'(x,y,z,t)$. The steric component of SSH is controlled by baroclinic motions, including balanced flows and IGWs. The non-steric component is controlled by barotropic motions.

Following Wang et al. (2018), we rearrange equation (1) to calculate the steric height from the total SSH, the atmospheric pressure and the bottom pressure:

$$\eta_{\text{steric}} = \eta - \frac{p_b'}{\rho_0 g} + \frac{p_a}{\rho_0 g} \tag{2}$$

The power spectrum of raw SSH is shown by the solid blue line and the steric height is shown by the red dashed line in figure 2. In both region A and region B, the tidal peaks are much less prominent in the steric SSH than in the raw SSH (compare blue and red lines in figure 2). The steric height still retains a peak at M_2 and S_2 frequencies, because the semidiurnal tide forces IGW motions at these frequencies.

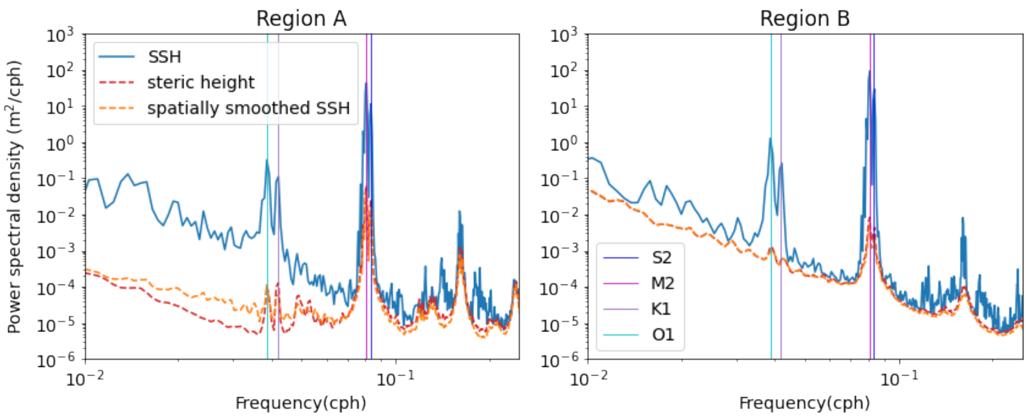

Figure 2. Power spectral density of the raw SSH (blue line), the steric height (red dashed line) and the SSH smoothed with a spatial filter (orange dashed line) in region A (left) and region B (right). Note that in region B the red dashed line is mostly obscured by the orange dashed line. Vertical lines mark the four highest-energy tidal frequencies, O_1, K_1, M_2, S_2.

Throughout the rest of this paper, whenever SSH is mentioned, the steric SSH is used. But we recognize that others may wish to apply our method to other kinds of data. If bottom pressure were not available, we could not calculate the steric height using equation (2). Because barotropic motions tend to have large spatial scales, we found that smoothing the SSH with a spatial filter (Grooms et al., 2021) that has a scale of 300km provides a good approximation of the steric height. The spectrum of the smoothed SSH is shown by the orange dashed line in figure 2.

2.2 Partitioning the wave and non-wave parts of the flow

2.2.1 ω-filtering

Frequency-based filtering, in which motions with frequencies lower than the inertial frequency are labelled as balanced and motions with frequencies higher than the inertial frequency are labelled as waves, is used as a baseline in this paper. This method has the main advantage of being very straightforward and computationally cheap. In our version of frequency filtering, we apply a convolution filter to the timeseries of velocity and steric SSH at each point in x, y, z. We choose to use a sinc function as the window function for this filter, because its Fourier transform is a top-hat (see e.g. Lilly and Lettvin (2004)), so the field after ω-filtering, ϕ_ω is given by

$$\phi_\omega(t) = \int_{t-t_w}^{t+t_w} \phi(t)\,\mathrm{sinc}\left(\frac{f(t-\tau)}{1.1\,\pi}\right)\,\mathrm{d}\tau\,, \tag{3}$$

where ϕ is the unfiltered field and $t_w = 36$ hours. The width of the sinc function is chosen to be $f/1.1$, where f is the local Coriolis parameter. This width is chosen so that near-inertial waves, which have frequencies close to f, will be removed by the filter, in addition to other IGWs with frequencies above f. Although the Fourier transform of a sinc function is a top-hat, ω-filtering does not completely remove all of the energies at frequencies higher than the inertial frequency because the sinc function is only applied over a 72-hour window: it is a good but imperfect low-pass filter.

2.2.2 Lagrangian filtering

As described above, Lagrangian filtering is a method where the filter is applied to a timeseries collected along the trajectory of a particle that moves with the horizontal flow field. Doppler shift has a negligible effect in the vertical direction (Shakespeare & Hogg, 2017), so horizontal advection of particles is sufficient. Lagrangian filtering requires computing Lagrangian trajectories from the Eulerian velocity field. We accomplish this by using the MITgcm FLT package, together with offline mode, to compute particle trajectories from the velocity fields stored on disk (see Code Repository for numerical details of the configuration.) At time t_{init}, particles are seeded at every grid point. Each particle is run forwards in time with a timestep of 25s from time t_{init} for 36 hours, and u, v, and η_{steric} are recorded along the trajectory of the particle. Each particle is also run backwards in time from time t_{init} for 36 hours, and u, v, and η_{steric} are recorded along the trajectory of the particle. The forward and backward trajectories are concatenated to form a single

72 hour long trajectory, for which the midpoint is the position of the particle at time t_{init}. This reseeding method was designed by Shakespeare et al. (2021) to prevent the particles from clustering around regions of convergence, which would bias the spatial sampling of the particles.

We choose to use the same filter window for Lagrangian filtering as for ω-filtering. For Lagrangian filtering, the sinc function window is applied to each 72-hour trajectory, with a new 72-hour trajectory generated every timestep, and then the filtered fields are concatenated in time, so the field after Lagrangian filtering, ϕ_{lf} is given by

$$\phi_{\mathrm{lf}}(t = t_{\mathrm{init}}) = \int_{-t_w}^{t_w} \phi_l(t_{\mathrm{init}}, \tau) \,\mathrm{sinc}\left(\frac{f\tau}{1.1\,\pi}\right) \mathrm{d}\tau\,, \tag{4}$$

where $\phi_l(t_{\mathrm{init}}, \tau)$ is the property field measured along particle trajectories initiated at time t_{init} and τ is the time the property recorded by each particle relative to its initialization time t_{init}.

Just as for ω-filtering above, the filter is a sinc function with width $f/1.1$, where f is the local Coriolis parameter for the position of the particle at time t_{init}. Our chosen filter is much sharper than the Butterworth filter used by Shakespeare et al. (2021): this means that our method removes more energy from waves than the Shakespeare et al. (2021) method.

2.2.3 ω-k filtering

Torres et al. (2018) propose a method of partitioning the balanced flow and the wave flow along a contour in frequency-wavenumber space. This contour is the dispersion curve of the tenth baroclinic mode: for a given wavenumber, the first nine baroclinic modes are found at higher frequencies than this contour (see figure 3 of Torres et al. (2018)). Torres et al. (2018) categorize motions with frequencies above the contour as waves, and motions with frequencies below the contour as balanced flow. In this paper, we refer to this method as ω-k filtering.

To perform ω-k filtering, we must transform the data from physical space to frequency-wavenumber space. A multidimensional Fourier transform only makes sense when all the dimensions are orthogonal, so we first project the field $\phi(\mathrm{lon}, \mathrm{lat}, t)$ in regions A and B from the sphere onto a tangent plane that is parallel to the Earth's surface at the center of each region. We then apply a Tukey window and Fourier-transform the field $\phi(x, y, t)$ to get $\phi(k_x, k_y, \omega)$. Frequencies higher than the tenth baroclinic mode are set to zero, and an inverse-Fourier transform is applied to the result. We then divide by the Tukey window to compensate for the reduction in energy associated with windowing. Because the Tukey window goes to zero at the beginning and end of the timeseries, and along the edges of the domain, in these regions, the results of ω-k filtering are very noisy. We chose to use a Tukey window because it has a large flat region across the center of the domain, in which windowing does not generate noise.

Because of the need to project onto a tangent plane, and the necessity of windowing, ω-k filtering is not well-suited for estimating the balanced flow over a large region of physical space. It is more suitable for application to small regions. Torres et al. (2018) use ω-k filtering to calculate the balanced and wave energy in frequency-wavenumber space for small regions of physical space, without attempting to inverse-transform back to physical space.

3 Results

3.1 Frequency spectrum

The power spectra described here were calculated from a two-week-long dataset of the filtered and unfiltered fields at hourly resolution (figure 3) For Lagrangian filtering, the filtering occurs in Lagrangian space, but the filtered velocities are transformed into Eulerian space before the spectrum is calculated. For all of the spectra, the unfiltered and filtered velocities are first averaged onto cell centers, and projected onto a tangent plane: this allows the results to be more easily compared with the frequency-wavenumber diagrams in section 3.2. The unfiltered, ω-filtered and Lagrangian filtered velocities are then used to calculate a power spectrum of speed, using all the points in each region. For ω-k filtering, the power spectrum is first calculated in frequency-wavenumber space, the filter is applied, and the result is summed over all wavenumbers to calculate the power spectrum as a function of frequency only.

The power spectrum of the horizontal speed in all three methods is shown in the top two panels of figure 3 We also computed rotary spectra (not shown), which reveal the difference between clockwise and counter-clockwise rotating flows, highlighting inertial oscillations. In these plots, for simplicity of presentation, we choose to focus just on the full spectrum, which is the sum of the clockwise and counter-clockwise components of the rotary spectrum. In region A, the unfiltered horizontal velocity field (the orange line in figure 3a) has a spectral peak at the inertial frequency (shown by the vertical black line in figure 3) and at the semidiurnal frequency (shown by the vertical blue line in figure 3), as well as additional peaks at various supertidal frequencies. These peaks are a feature of high-resolution global models, perhaps caused by insufficient resolution of internal wave triads (Savage et al., 2017; Arbic et al., 2022). These peaks are associated with inertia-gravity waves in LLC4320 (Torres et al., 2018).

Overall, there is more energy at high frequencies in region B than in region A. In region B, the spectrum of the unfiltered horizontal velocity has a small peak at the semidiurnal frequency, but does not have other peaks at higher tidal frequencies (orange line in figure 3b). The spectrum of unfiltered steric SSH also has smaller peaks in region B than in region A (compare the orange lines in figure 3c and figure 3d). This suggests that a larger fraction of the total energy in region A is in IGWs.

In both regions, all three filtering methods reduce the high frequency energy of the horizontal velocity field, but ω-filtering removes the most energy from these frequencies (red dashed line in all panels of figure 3). Although they use exactly the same window function in their filter, there is a significant difference between the results of ω-filtering and the results of Lagrangian filtering. In fact at higher frequencies, Lagrangian filtering retains the most superinertial energy of all the filtering methods. Recall that the spectra presented here were calculated in Eulerian space. Lagrangian filtering is designed to remove energy at frequencies above the inertial frequency in a coordinate following the flow. Hence, energy that remains after Lagrangian filtering must be at subinertial frequencies in the Lagrangian frame, and must be Doppler-shifted into the superinertial range by velocities that change on longer timescales. The logarithmic scale and high energy of the flow at subinertial frequencies means small differences in the subinertial energy are not visible in this figure: it is possible that an equal amount of energy that appears subinertial in the reference frame of the Earth but is superinertial in the reference frame of the flow is removed by Lagrangian filtering. This is explored further in section 3.2.

The ω-k-filtered spectrum retains more energy at subinertial frequencies than other methods, because the filter only removes frequencies higher than the 10th baroclinic mode. The roll-off of the ω-filter and Lagrangian filter are specifically designed to remove waves with intrinsic frequencies close to f, because we do not expect near-inertial waves to contribute to tracer transport.

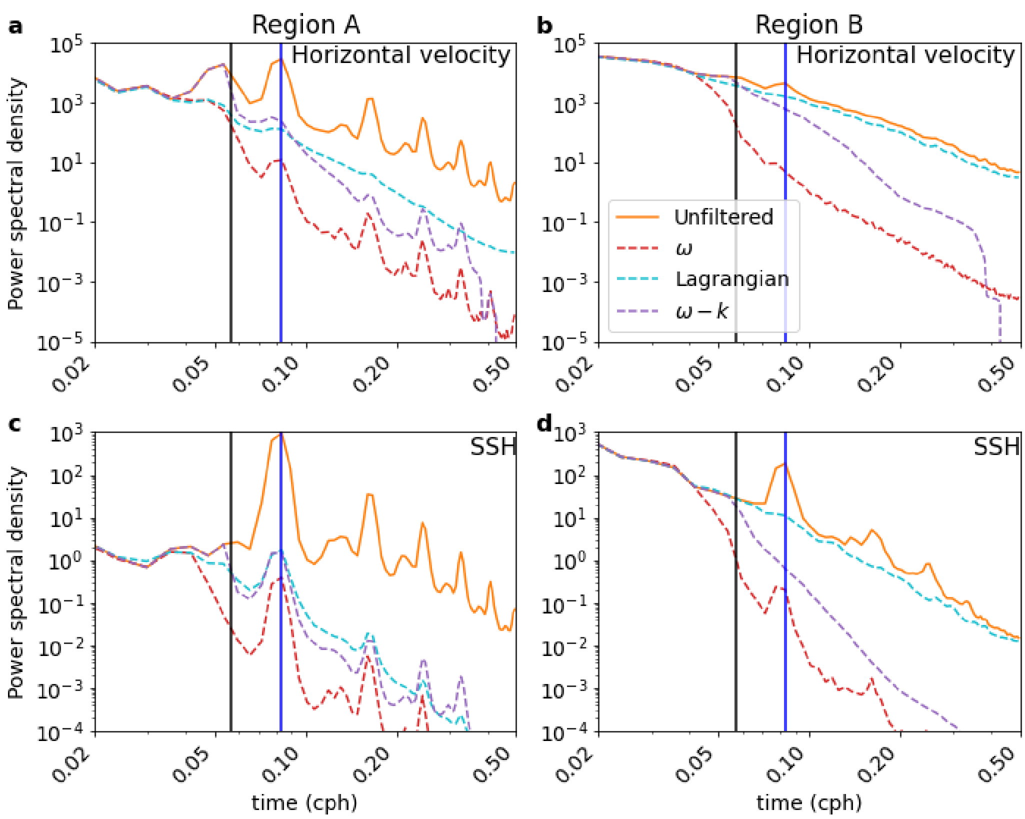

Figure 3. a) Power spectrum of horizontal velocity field calculated from the flow in region A, and b) power spectrum of horizontal velocity field calculated from the flow in region B. c) Power spectrum of SSH field calculated from the flow in region A and d) power spectrum of horizontal velocity field calculated from the flow in region B. In each panel, the orange solid line is the spectrum of the unfiltered field, the red dashed line is the spectrum of the ω-filtered field, the cyan dashed line is the spectrum of the Lagrangian filtered field and the purple dashed line is the spectrum of the ω-k filtered field. The vertical black line is the inertial frequency and the vertical blue line is the semidiurnal frequency.

In region A, the spectrum of the Lagrangian-filtered horizontal velocity has none of the peaks that are associated with IGWs in LLC4320, and only a small peak at the inertial frequency (cyan line in figure 3a). One interpretation of this result is that Lagrangian filtering is removing the IGW energy in the horizontal velocity field, including the energy concentrated at the tidal harmonics. ω-k filtering removes less energy than ω-filtering, but it still reduces the energy at high frequencies by more than an order of magnitude (purple dashed line in figure 3b). Lagrangian filtering also removes the tidal peaks in the unfiltered

SSH spectrum in region B (cyan line in figure 3d), but most of the high-frequency energy in the velocity field is retained (cyan line in figure 3b). One potential explanation is that Lagrangian filtering is mostly removing IGW energy in the SSH field in region B, but that most of the superinertial energy in region B comes from low-frequency motions that have been Doppler shifted into the superinertial range.

3.2 Frequency-wavenumber spectra

The frequency spectrum summarizes a lot of information about the flow, but to better understand the characteristics of each of the filtering methods, it is helpful to calculate the power spectrum in frequency-wavenumber space. Figure 4 shows the isotropic frequency-wavenumber diagram for the surface velocity in region A and figure 5 shows the same analysis for region B. The unfiltered velocities (figures 4a and 5a) contain more low-frequency energy in region B. In region A, the energy at frequencies higher than the 10th baroclinic mode (shown by the green contour) is concentrated in discrete bands, which suggests that this energy is associated with IGWs. In region B, the most of the energy at frequencies higher than the 10th baroclinic mode is smoothly connected to the energy at lower frequencies.

It is important to remember that these frequency-wavenumber diagrams are a representation of the amount of energy at each frequency and wavenumber measured in Eulerian space (regardless of what kind of filtering is applied). It is not feasible to calculate a frequency-wavenumber diagram in Lagrangian space, so the Lagrangian-filtered velocities are operated on in Eulerian space to create this diagram.

As expected, ω-filtering removes most of the energy at frequencies higher than the inertial frequency (figures 4b and 5b). However, as above, Lagrangian filtering preserves a lot of energy with frequencies higher than the inertial frequency in the Eulerian frame. The energy that is preserved by Lagrangian filtering generally has large wavenumbers.

The figures 4e and 5e show the difference between the frequency-wavenumber spectrum with Lagrangian filtering and the frequency-wavenumber spectrum with ω-filtering. In both regions, the Lagrangian-filtered velocities have more energy at superinertial frequencies in the Eulerian frame and less energy at subinertial frequencies in the Eulerian frame. This indicates that Doppler shifting is likely happening in both directions: ω-filtering spuriously removes flow that is Doppler shifted into the superinertial range, and spuriously retains flow that is Doppler shifted into the subinertial range.

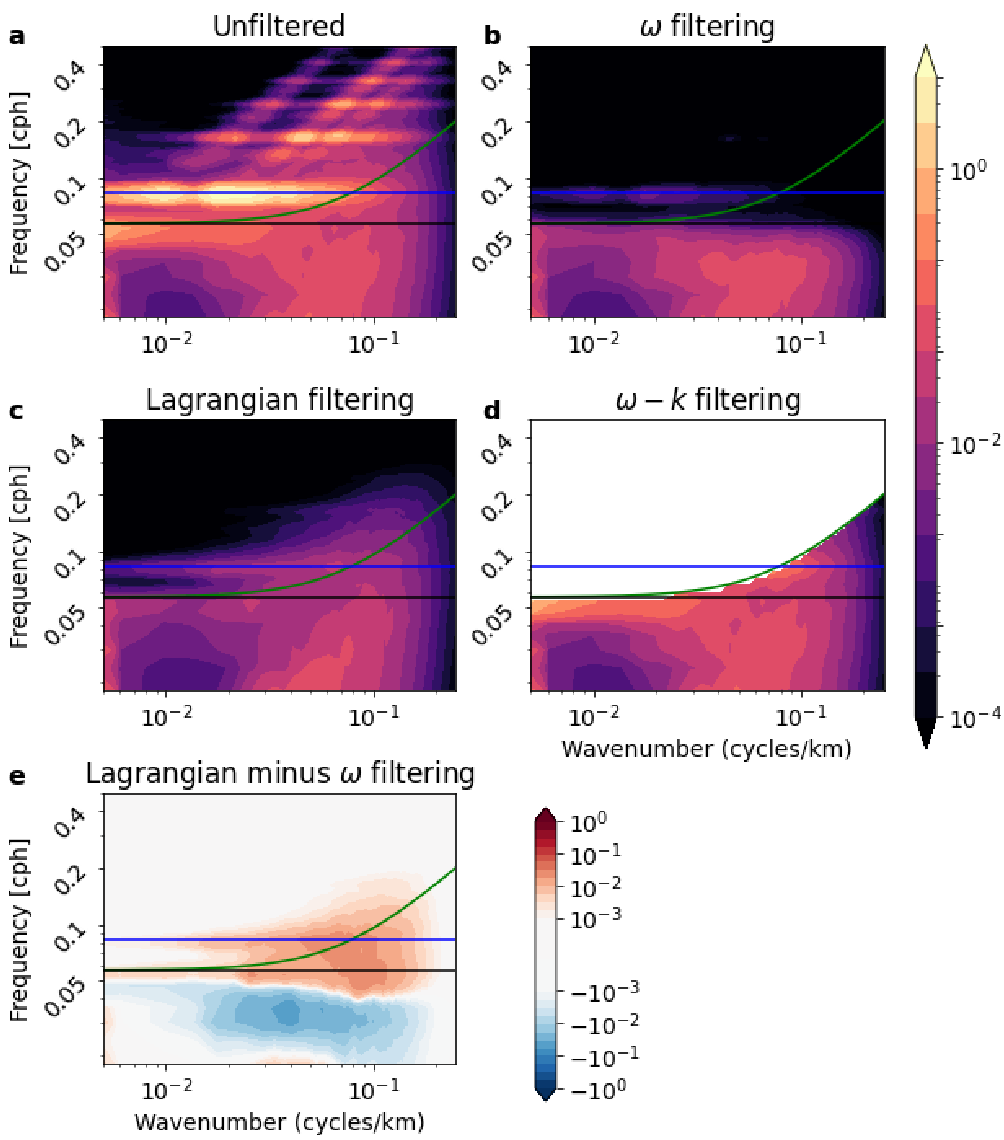

Figure 4. The isotropic frequency-wavenumber spectrum of horizontal velocity field calculated from the flow inside region A, the blue box of figure 1, for a) the unfiltered velocity field, b) the ω-filtered velocity, c)the Lagrangian filtered velocity and d) the ω-k filtered velocity. e) The frequency-wavenumber spectrum of Lagrangian filtered horizontal velocity minus the frequency-wavenumber spectrum of the ω-filtered velocity. The black horizontal line is the inertial frequency and the blue horizontal line is the semidiurnal frequency. The green line is the tenth baroclinic mode. The isotropic frequency-wavenumber spectrum is obtained by azimuthally-averaging over all values of k, where $k = \sqrt{k_x^2 + k_y^2}$.

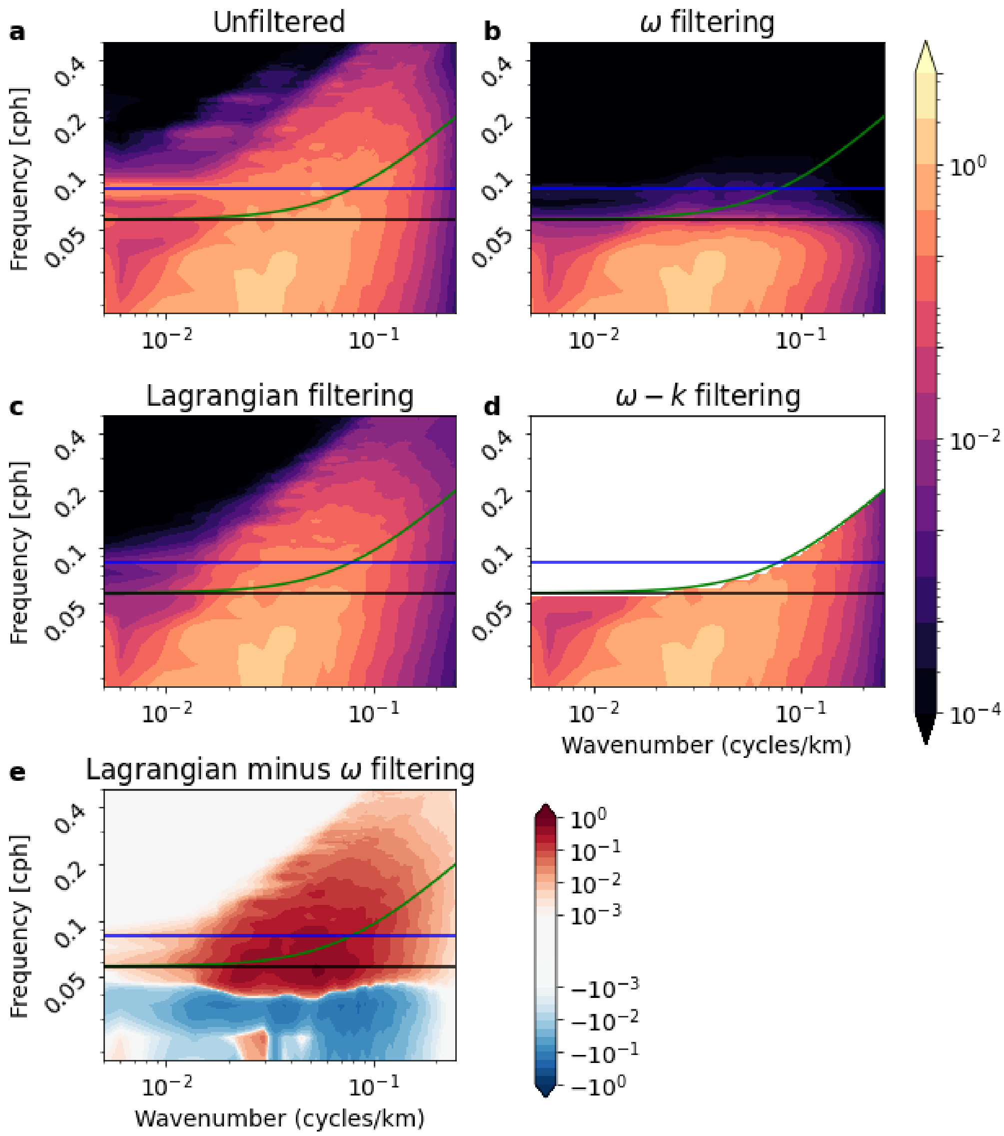

Figure 5. The isotropic frequency-wavenumber spectrum of horizontal velocity field calculated from the flow inside region B, the green box of figure 1, for a) the unfiltered velocity field, b) the ω-filtered velocity, c) the Lagrangian filtered velocity and d) the ω-k filtered velocity. e) The frequency-wavenumber spectrum of Lagrangian filtered horizontal velocity minus the frequency-wavenumber spectrum of the ω-filtered velocity. The black horizontal line is the inertial frequency and the blue horizontal line is the semidiurnal frequency. The green line is the tenth baroclinic mode. The isotropic frequency-wavenumber spectrum is obtained by azimuthally-averaging over all values of k, where $k = \sqrt{k_x^2 + k_y^2}$.

The frequency-wavenumber diagram after ω-k filtering is shown in the figures 4d and 5d for comparison with Lagrangian filtering. ω-k filtering removes a large amount of super-inertial energy in both region A and region B. Lagrangian filtering retains much more of the low- to intermediate-wavenumber super-inertial energy in region B, suggesting that much of this energy is associated with balanced flow that has been Doppler-shifted into the super-inertial range. Region B is characterized by stronger currents, so more pronounced Doppler shift is expected.

3.3 Vorticity-strain JPDFs

One way to evaluate the separation of wave velocity and balanced velocity is by considering the joint probability density function (JPDF) of the normalized-by-f surface vorticity ζ/f, strain $\sigma/|f|$, and divergence δ/f, where

$$\zeta = v_x - u_y \tag{5}$$

$$\sigma = \sqrt{(u_x - v_y)^2 + (v_x + u_y)^2} \tag{6}$$

$$\delta = u_x + v_y. \tag{7}$$

Balwada et al. (2021) found that the vorticity-strain JPDFs of submesoscale-rich flows are characterized by a clear frontal signature, appearing as concentrations along the ± 1 slope lines, because $|\zeta| \approx \sigma$ for fronts. Moreover, because large frontal vertical velocities generate vortex stretching in the vorticity equation, submesoscale fronts are highly asymmetric and skewed toward positive vorticity, which appears as a long tail on the cyclonic side of the JPDF.

By contrast, wave-dominated super-inertial flows tend to have $|\zeta| \ll |\delta| \sim \sigma$ and lack an asymmetry-generating mechanism, and thus have vorticity-strain JPDFs that are mostly symmetric and centered around the origin. Consider, for example, a shallow water inertia-gravity wave, which has $\zeta = f|\mathbf{k}|/\omega \cos\theta$ and $\delta = |\mathbf{k}| \sin\theta$, where $\mathbf{k}$ is the horizontal wavenumber and $\theta = \mathbf{k}\cdot\mathbf{x} - \omega t$. Thus $\zeta/\delta \sim f/\omega$, so that for high-frequency waves, $|\zeta| \ll |\delta|$. Moreover, $\sigma = \sqrt{\zeta^2 + \delta^2}$, so for high-frequency waves, $\sigma \sim |\delta|$. Thus by considering the vorticity-strain JPDFs calculated from the filtered and unfiltered velocity fields, we can get a sense of how well the various filtering methods preserve frontal features and remove waves.

Figure 6 shows, for regions A and B, the vorticity-strain JPDFs of the unfiltered velocity, the ω-filtered velocity, the Lagrangian-filtered velocity, and the unfiltered-minus-filtered velocity fields for each filtering method (specifically, we compute the JPDFs of the velocity field obtained by subtracting the filtered from the unfiltered velocity). The unfiltered-minus-filtered velocity fields represents the IGW part as inferred by each method. The JPDF of the unfiltered velocity is more asymmetric and extends much farther along the $\zeta = \sigma$ line in region B than in region A, consistent with the former being characterized by higher energy and more submesoscale fronts (compare the panels in the top row of figure 6). The JPDFs of the unfiltered velocity fields for each region share roughly the same shapes with their filtered velocity fields, using any filtering method, indicating that both the filtered and unfiltered velocity fields contain some balanced flows associated with fronts.

The JPDFs of the unfiltered-minus-filtered velocities (i.e. the velocities categorized as waves) are different between filtering methods. In region A, the JPDFs are relatively symmetric, indicating that very few submesoscale fronts are mis-categorized as wave-like. However, in region B, the JPDF of the unfiltered-minus-filtered flow are asymmetric for ω-filtering and ω-k filtering, but symmetric with Lagrangian-filtering. This suggests that, at least in region B, where balanced ageostrophic flows are strong, ω-filtering and ω-k filtering spuriously filters out parts of the balanced flow (mis-categorizing them as wave-like), while Lagrangian filtering does not. Moreover, in both regions, ω-filtering removes larger vorticity and strain values, while Lagrangian-filtering preserves them. These JPDFs provide additional evidence that in both regions, Lagrangian filtering is more effective at removing waves, while preserving balanced ageostrophic flows, than ω-filtering.

3.4 Divergence in physical space

The horizontal velocities associated with waves are more divergent than the horizontal velocities associated with geostrophically-balanced flows (see e.g. Bühler et al. (2014)). However, upper-ocean submesoscale flows are characterized by strongly convergent fronts. An important test of filtering methods is the degree to which they retain the divergence associated with submesoscale fronts while removing the divergence associated with wave-like flows. We show the divergence of the surface velocity field for a representative time snapshot in figure 7 (region A) and in figure 8 (region B). We also plot the frontogenesis function,

$$F_s = \mathbf{Q}_s \cdot \nabla_h b \,, \tag{8}$$

where $\mathbf{Q}_s = -\left(\frac{\partial u}{\partial x}\frac{\partial b}{\partial x} + \frac{\partial v}{\partial x}\frac{\partial b}{\partial y} + \frac{\partial w}{\partial x}\frac{\partial b}{\partial z}, \frac{\partial u}{\partial y}\frac{\partial b}{\partial x} + \frac{\partial v}{\partial y}\frac{\partial b}{\partial y} + \frac{\partial w}{\partial y}\frac{\partial b}{\partial z}\right)$. Large positive values indicate that the flow field is acting to increase the buoyancy gradient (Hoskins, 1982; Capet et al., 2008; Brannigan et al., 2015). Hence, these large values tend to be present at fronts.

Here, we compare the divergence field with the frontogenesis function: we expect that regions with high convergence associated with fronts will be associated with high values of the frontogenesis function. Of course, the frontogenesis function may not be high for all balanced convergent or divergent features, and not all such features are necessarily fronts.

Figures 7 and 8 show that ω-filtering, Lagrangian filtering and ω-k filtering all reduce the divergence of the velocity field significantly. In region A, ω-filtering and Lagrangian filtering reduce the divergence more than ω-k filtering (compare figure 7b, c, and d with figure 7a), even in regions with a low frontogenesis function. This suggests that ω-k filtering does not remove all the waves. Both ω-filtering and Lagrangian filtering preserve higher divergences and convergences close to regions where the frontogenesis function is large and positive (the region surrounded by a thin black contour). Figures 7e,f show magnified parts of regions A where this effect is visible.

In region B, ω-filtering reduces the divergence the most out of all the filtering methods (Figure 8b). Lagrangian filtering preserves much more negative divergences in the region where the frontogenesis function is large and positive (Figure 8c,e,f). This suggests that in region B, Lagrangian filtering preserves more of the ageostrophically-balanced flow associated with convergent fronts.

3.5 Geostrophy

Across most of the ocean, surface velocities that are estimated by applying geostrophy to the unfiltered sea-surface height field are not good predictors of the true sea-surface velocity field (Yu et al., 2021). Removing the inertia gravity wave signal removes velocities that are not in geostrophic balance, so we might expect that the filtered velocities will be more geostrophic than the unfiltered velocities. In figure 9, we estimate the geostrophic velocity by naively applying the geostrophic equation to the sea-surface-height field, and then take the root-mean-square difference between the surface speed and this SSH-derived geostrophic speed estimate:

$$\mathrm{RMS}^{ij} = \frac{1}{A}\int \frac{\sqrt{\left(\frac{1}{T}\int(|\mathbf{v}^i| - |\mathbf{v}^j_{\mathrm{ssh}}|)^2\,\mathrm{d}t\right)}}{\sigma_t(|\mathbf{v}^i|)}\,dA\,, \tag{9}$$

where $\mathbf{v}$ is the velocity at the surface, i is the type of filtering used on the velocity field (no filtering, ω-filtering, Lagrangian filtering or ω-k filtering), $\mathbf{v}_{\text{ssh}}$ is the SSH-derived velocity field, j is the type of filtering used on the SSH field, and T is the total length of the timeseries after filtering (70days). We normalize this root-mean-square difference by the pointwise standard deviation of the velocity field, $\sigma_t(|\mathbf{v}^i|)$.

The raw-SSH-derived geostrophic velocity field is based on the unfiltered steric SSH, so it contains a significant amount of variability from waves. Applying a filter to the SSH before creating the SSH-derived geostrophic velocity estimates leads to marginally better agreement between the velocity field and the SSH-derived velocity field in region A (compare bottom row of the left panel of figure 9 with earlier rows). This suggests that the SSH is strongly influenced by high frequency motions which are not geostrophic. Even though Lagrangian filtering may preserve more of the balanced flow at high frequencies, Lagrangian filtering is no better than ω-filtering for picking out geostrophic balance in region A. Hence, the high frequency flow that is preserved by Lagrangian filtering is mostly not in geostrophic balance.

In region B, filtering the velocity field does not significantly improve its agreement with the raw-SSH-derived geostrophic velocity estimate (bottom row of right panel in figure 9). This is probably because region B contains a lot of submesoscale activity and most of the balanced flows in region B are ageostrophic. Applying an ω-filter or ω-k filter to the SSH field leads to more agreement between SSH-derived velocity estimate and the surface velocities: both of these filters remove high frequency motions of all kinds from the SSH field. Applying a Lagrangian filter to the SSH is generally less effective at picking out geostrophy, suggesting that a lot of the motion preserved by Lagrangian filtering in region B is not geostrophic (even if it is balanced).

Regions A and B are in two different regimes, but the Rossby number is relatively high in both regions. Geostrophy is not an effective way to calculate surface velocities from sea-surface height in either regime. Applying geostrophic balance to SWOT measurements at small scales is unlikely to be an effective way to calculate ocean surface velocities, even after filtering is applied. This is an important difference from previous satellite altimetry missions.

4 Conclusions

SWOT offers an unprecedented opportunity to observe the global sea surface height down to scales of O(10 km), an order of magnitude improvement over the current generation of altimeters (Fu and Ferrari, 2008). While at coarser scales, geostrophic balance allows accurate estimation of upper-ocean velocity from SSH, no such simple balance can be used to extract velocities from SWOT measurements. The lack of a simple balance to relate SSH to velocities poses not only a challenge to determining the latter, it also implies that the velocity field itself is more complex at these scales. In particular, it will contain components due to both ageostrophic balances, as well as inertia-gravity wave signals. The latter do not impact tracer transport, but act as noise that complicates studies of the relationship between the SSH and the transport-relevant velocity field.

Here we have investigated an approach to solving one part of the complex puzzle posed by SWOT data: filtering wave signals from high-resolution data. The methods considered include simple low-pass filtering in frequency (termed ω-filtering), combined wavenumber-frequency filtering (ω-k filtering, after Torres et al. (2018)), and Lagrangian filtering (after Shakespeare and Hogg (2017); Shakespeare et al. (2021)).

ω-filtering is computationally very cheap, and it removes all motions at frequencies higher then f in the Eulerian frame from the surface velocity field. However, this process removes some motions that have been Doppler shifted to higher frequencies, including some motions associated with fronts and filaments. ω-k filtering, which was proposed by Torres et al. (2018), was designed based on the frequency-wavenumber properties of flow in the Kuroshio Extension region. Frequencies higher than the tenth baroclinic mode were observed to fall in discrete bands, suggesting they were associated with IGWs. This paper shows that in region B (a region with strong mesoscale flows), this is not true: much of the energy at frequencies higher than the tenth baroclinic mode appears smooth in the frequency-wavenumber diagram shown in figure 5. The use of the tenth baroclinic mode works relatively well in our region A, but it is unlikely to be useful for partitioning the flow in regions with strong mesoscale currents. Although ω-k filtering is computationally cheaper than Lagrangian filtering, we do not think that it is applicable in all regions of the ocean.

We show that in region B, lagrangian filtering preserves a lot of motions that appear superinertial in the reference frame of the Earth, but are subinertial in the reference frame of the flow. This is consistent with previous work by Callies et al. (2020), which showed that the velocity field observed at a fixed location in the North Atlantic is predominantly rotational even at apparently superinertial frequencies. Callies et al. (2020) hypothesized that they were observing balanced flow that was Doppler shifter into the superinertial range. In this paper we confirm that surface velocities in the superinertial range include Doppler-shifted motions, at least in the LLC4320 simulation.

In high-energy regions, Lagrangian filtering appears to be more likely to preserve flows close to filaments and fronts. It is likely that these flows are ageostrophically balanced. In realistic simulations (and in the ocean itself), there is not a clean metric to evaluate whether velocities are balanced, but we make use of the frontogenesis function and vorticity-strain JPDFs to understand the features of the velocities that are preserved by Lagrangian filtering. We show that it particularly preserves convergent flows in areas of frontogenesis. Preserving these convergent flows is likely to be important for modeling the vertical transport of ocean tracers. The differences between Lagrangian filtering and the other methods are larger in regions with high energy flows, like our region B, and smaller in regions without large-scale background flows, like our region A. More research is needed to identify when Lagrangian filtering is likely to be useful, and when it is an unnecessary computational expense.

Lagrangian filtering also removes motions that appear subinertial in the reference frame of the Earth, but are superinertial in the reference frame of the flow. This has not been observed before but consistent with the effects of Doppler shift hypothesized by Pinkel (2008). Because IGWs generally have lower energies than balanced motions, Doppler shifted IGWs do not have much effect on the total energy measured in the subinertial range.

We do not expect that the methods described here will be directly applied to SWOT observations. This paper represents the first step in the journey to extract the transport-relevant velocity field from high-resolution SSH observations. With these new insights about how to isolate balanced motions from the full velocity and SSH fields, we intend to create a large dataset that contains snapshots of filtered SSH, together with the filtered surface velocity field associated with each SSH snapshot. This dataset can then be used as a truth signal which can be used to define a supervised machine-learning problem for extracting the transport-relevant velocity field from low temporal resolution SSH snapshots. The method that is developed may then be applied to SWOT observations, finally leading to estimates ocean surface velocities.

This multistep process is involved, but has the potential to produce surface velocity data with high value to the scientific community. Alongside this approach, we advocate the use of intermediate approaches like using vorticity-strain joint PDFs (Balwada et al., 2021) to short-circuit directly to inference of transport-active flow from velocity, even with waves in latter.

5 Open Research

The code repository for this work is at `https://github.com/cspencerjones/separating-balanced`. The datasets used to create figures 3-7 are available at `https://doi.org/10.5281/zenodo.7495109` (Jones et al., 2022). Figures 1 and 2 can be created from the LLC4320 data that is available via the pangeo catalog: `https://catalog.pangeo.io/browse/master/ocean/LLC4320/`.

Acknowledgments

All authors acknowledge support from NASA award 80NSSC20K1142. This work would not have been possible without the tools provided by and maintained by the Pangeo community (https://pangeo.io/).

References

Abernathey, R. P., & Marshall, J. (2013). Global surface eddy diffusivities derived from satellite altimetry. *Journal of Geophysical Research: Oceans*, *118*(2), 901–916.

Arbic, B. K., Elipot, S., Brasch, J. M., Menemenlis, D., Ponte, A. L., Shriver, J. F., . . . others (2022). Near-surface oceanic kinetic energy distributions from drifter observations and numerical models. *Journal of Geophysical Research: Oceans*, *127*(10), e2022JC018551.

Balwada, D., Smith, K. S., & Abernathey, R. (2018). Submesoscale vertical velocities enhance tracer subduction in an idealized antarctic circumpolar current. *Geophysical Research Letters*, *45*(18), 9790–9802.

Balwada, D., Xiao, Q., Smith, S., Abernathey, R., & Gray, A. R. (2021). Vertical fluxes conditioned on vorticity and strain reveal submesoscale ventilation. *Journal of Physical Oceanography*.

Barton, A. D., Dutkiewicz, S., Flierl, G., Bragg, J., & Follows, M. J. (2010). Patterns of diversity in marine phytoplankton. *Science*, *327*(5972), 1509–1511.

Brannigan, L., Marshall, D. P., Naveira-Garabato, A., & Nurser, A. G. (2015). The seasonal cycle of submesoscale flows. *Ocean Modelling*, *92*, 69–84.

Bühler, O., Callies, J., & Ferrari, R. (2014). Wave–vortex decomposition of one-dimensional ship-track data. *Journal of Fluid Mechanics*, *756*, 1007–1026.

Buijsman, M. C., Stephenson, G. R., Ansong, J. K., Arbic, B. K., Green, J. M., Richman, J. G., … Zhao, Z. (2020). On the interplay between horizontal resolution and wave drag and their effect on tidal baroclinic mode waves in realistic global ocean simulations. *Ocean Modelling*, *152*, 101656.

Callies, J., Barkan, R., & Garabato, A. N. (2020). Time scales of submesoscale flow inferred from a mooring array. *Journal of Physical Oceanography*, *50*(4), 1065–1086.

Capet, X., McWilliams, J. C., Molemaker, M. J., & Shchepetkin, A. (2008). Mesoscale to submesoscale transition in the california current system. part ii: Frontal processes. *Journal of Physical Oceanography*, *38*(1), 44–64.

Caspar-Cohen, Z., Ponte, A., Lahaye, N., Carton, X., Yu, X., & Le Gentil, S. (2022). Characterization of internal tide incoherence: Eulerian versus lagrangian perspectives. *Journal of Physical Oceanography*.

Chouksey, M., Eden, C., & Brüggemann, N. (2018). Internal gravity wave emission in different dynamical regimes. *Journal of Physical Oceanography*, *48*(8), 1709–1730.

Cronin, M. F., Gentemann, C. L., Edson, J., Ueki, I., Bourassa, M., Brown, S., … others (2019). Air-sea fluxes with a focus on heat and momentum. *Frontiers in Marine Science*, 430.

Ducet, N., Le Traon, P.-Y., & Reverdin, G. (2000). Global high-resolution mapping of ocean circulation from topex/poseidon and ers-1 and-2. *Journal of Geophysical Research: Oceans*, *105*(C8), 19477–19498.

Eden, C., Chouksey, M., & Olbers, D. (2019). Gravity wave emission by shear instability. *Journal of Physical Oceanography*, *49*(9), 2393–2406.

Egbert, G. D., Bennett, A. F., & Foreman, M. G. (1994). Topex/poseidon tides estimated using a global inverse model. *Journal of Geophysical Research: Oceans*, *99*(C12), 24821–24852.

Egbert, G. D., & Erofeeva, S. Y. (2002). Efficient inverse modeling of barotropic ocean tides. *Journal of Atmospheric and Oceanic technology*, *19*(2), 183–204.

Elipot, S., Lumpkin, R., Perez, R. C., Lilly, J. M., Early, J. J., & Sykulski, A. M. (2016). A global surface drifter data set at hourly resolution. *Journal of Geophysical Research:*

Oceans, *121*(5), 2937–2966.

Elipot, S., & Wenegrat, J. (2021). Vertical structure of near-surface currents–importance, state of knowledge, and measurement challenges.

Ferrari, R. (2011). A frontal challenge for climate models. *Science*, *332*(6027), 316–317.

Furuichi, N., Hibiya, T., & Niwa, Y. (2008). Model-predicted distribution of wind-induced internal wave energy in the world's oceans. *Journal of Geophysical Research: Oceans*, *113*(C9).

Grooms, I., Loose, N., Abernathey, R., Steinberg, J., Bachman, S. D., Marques, G., … Yankovsky, E. (2021). Diffusion-based smoothers for spatial filtering of gridded geophysical data. *Journal of Advances in Modeling Earth Systems*, *13*(9), e2021MS002552.

Hoskins, B. J. (1982). The mathematical theory of frontogenesis. *Annual review of fluid mechanics*, *14*(1), 131–151.

Jones, C. S., Xiao, Q., Abernathey, R. P., & Smith, K. S. (2022). *A dataset for comparing filtering methods used to wave and non-wave flow at the surface of the agulhas region* [dataset]. Zenodo. doi: 10.5281/zenodo.7495109

Kafiabad, H. A., & Bartello, P. (2016). Balance dynamics in rotating stratified turbulence. *Journal of Fluid Mechanics*, *795*, 914–949.

Klein, P., Lapeyre, G., Siegelman, L., Qiu, B., Fu, L.-L., Torres, H., … Le Gentil, S. (2019). Ocean-scale interactions from space. *Earth and Space Science*, *6*(5), 795–817.

Lahaye, N., Gula, J., & Roullet, G. (2019). Sea surface signature of internal tides. *Geophysical Research Letters*, *46*(7), 3880–3890.

Lévy, M., Franks, P. J., & Smith, K. S. (2018). The role of submesoscale currents in structuring marine ecosystems. *Nature communications*, *9*(1), 1–16.

Lilly, J. M., & Lettvin, E. (2004). The "switch-on" problem for linear time-invariant operators. *Signal processing*, *84*(4), 763–784.

Luecke, C. A., Arbic, B. K., Richman, J. G., Shriver, J. F., Alford, M. H., Ansong, J. K., … others (2020). Statistical comparisons of temperature variance and kinetic energy in global ocean models and observations: Results from mesoscale to internal wave frequencies. *Journal of Geophysical Research: Oceans*, *125*(5), e2019JC015306.

Mahadevan, A., Pascual, A., Rudnick, D. L., Ruiz, S., Tintoré, J., & D'Asaro, E. (2020). Coherent pathways for vertical transport from the surface ocean to interior. *Bulletin of the American Meteorological Society*, *101*(11), E1996–E2004.

Masur, G. T., & Oliver, M. (2020). Optimal balance for rotating shallow water in primitive variables. *Geophysical & Astrophysical Fluid Dynamics*, *114*(4-5), 429–452.

Mazloff, M. R., Cornuelle, B., Gille, S. T., & Wang, J. (2020). The importance of remote forcing for regional modeling of internal waves. *Journal of Geophysical Research: Oceans*, *125*(2), e2019JC015623.

Mkhinini, N., Coimbra, A. L. S., Stegner, A., Arsouze, T., Taupier-Letage, I., & Béranger, K. (2014). Long-lived mesoscale eddies in the eastern mediterranean sea: Analysis of 20 years of aviso geostrophic velocities. *Journal of Geophysical Research: Oceans*, *119*(12), 8603–8626.

Morrow, R., Fu, L.-L., Ardhuin, F., Benkiran, M., Chapron, B., Cosme, E., ... others (2019). Global observations of fine-scale ocean surface topography with the surface water and ocean topography (swot) mission. *Frontiers in Marine Science*, *6*, 232.

Niiler, P., Maximenko, N., Panteleev, G., Yamagata, T., & Olson, D. (2003). Near-surface dynamical structure of the kuroshio extension. *Journal of Geophysical Research: Oceans*, *108*(C6).

Nwankwo, U., Howden, S., Nechaev, D., & Dzwonkowski, B. (2023). Subinertial sea surface heights anomalies estimated using high frequency radar surface current data in the mississippi bight. *Journal of Geophysical Research: Oceans*, e2022JC019055.

Onuki, Y. (2020). Quasi-local method of wave decomposition in a slowly varying medium. *Journal of Fluid Mechanics*, *883*.

Pinkel, R. (2008). Advection, phase distortion, and the frequency spectrum of finescale fields in the sea. *Journal of physical oceanography*, *38*(2), 291–313.

Plumb, R. (1979). Eddy fluxes of conserved quantities by small-amplitude waves. *Journal of atmospheric sciences*, *36*(9), 1699–1704.

Ponte, A. L., Klein, P., Dunphy, M., & Le Gentil, S. (2017). Low-mode internal tides and balanced dynamics disentanglement in altimetric observations: Synergy with surface density observations. *Journal of Geophysical Research: Oceans*, *122*(3), 2143–2155.

Qiu, B., Chen, S., Klein, P., Torres, H., Wang, J., Fu, L.-L., & Menemenlis, D. (2020). Reconstructing upper-ocean vertical velocity field from sea surface height in the presence of unbalanced motion. *Journal of Physical Oceanography*, *50*(1), 55–79.

Resplandy, L., Lévy, M., Madec, G., Pous, S., Aumont, O., & Kumar, D. (2011). Contribution of mesoscale processes to nutrient budgets in the arabian sea. *Journal of Geophysical Research: Oceans*, *116*(C11).

Richman, J. G., Arbic, B. K., Shriver, J. F., Metzger, E. J., & Wallcraft, A. J. (2012). Inferring dynamics from the wavenumber spectra of an eddying global ocean model with embedded tides. *Journal of Geophysical Research: Oceans*, *117*(C12).

Rocha, C. B., Gille, S. T., Chereskin, T. K., & Menemenlis, D. (2016). Seasonality of submesoscale dynamics in the kuroshio extension. *Geophysical Research Letters*, *43*(21), 11–304.

Savage, A. C., Arbic, B. K., Alford, M. H., Ansong, J. K., Farrar, J. T., Menemenlis, D., … others (2017). Spectral decomposition of internal gravity wave sea surface height in global models. *Journal of Geophysical Research: Oceans*, *122*(10), 7803–7821.

Shakespeare, C. J., Gibson, A. H., Hogg, A. M., Bachman, S. D., Keating, S. R., & Velzeboer, N. (2021). A new open source implementation of lagrangian filtering: A method to identify internal waves in high-resolution simulations. *Journal of Advances in Modeling Earth Systems*, *13*(10), e2021MS002616.

Shakespeare, C. J., & Hogg, A. M. (2017). Spontaneous surface generation and interior amplification of internal waves in a regional-scale ocean model. *Journal of Physical Oceanography*, *47*(4), 811–826.

Sinha, A., Balwada, D., Tarshish, N., & Abernathey, R. (2019). Modulation of lateral transport by submesoscale flows and inertia-gravity waves. *Journal of Advances in Modeling Earth Systems*, *11*(4), 1039–1065.

Stammer, D., Ray, R., Andersen, O. B., Arbic, B., Bosch, W., Carrère, L., … others (2014). Accuracy assessment of global barotropic ocean tide models. *Reviews of Geophysics*, *52*(3), 243–282.

Torres, H. S., Klein, P., Menemenlis, D., Qiu, B., Su, Z., Wang, J., … Fu, L.-L. (2018). Partitioning ocean motions into balanced motions and internal gravity waves: A modeling study in anticipation of future space missions. *Journal of Geophysical Research: Oceans*, *123*(11), 8084–8105.

Uchida, T., Balwada, D., P Abernathey, R., A McKinley, G., K Smith, S., & Lévy, M. (2020). Vertical eddy iron fluxes support primary production in the open southern ocean. *Nature communications*, *11*(1), 1–8.

Van Sebille, E., Aliani, S., Law, K. L., Maximenko, N., Alsina, J. M., Bagaev, A., … others (2020). The physical oceanography of the transport of floating marine debris. *Environmental Research Letters*, *15*(2), 023003.

Viúdez, Á., & Dritschel, D. G. (2004). Optimal potential vorticity balance of geophysical flows. *Journal of Fluid Mechanics*, *521*, 343–352.

Wang, J., Fu, L.-L., Qiu, B., Menemenlis, D., Farrar, J. T., Chao, Y., … Flexas, M. M. (2018). An observing system simulation experiment for the calibration and validation of the surface water ocean topography sea surface height measurement using in situ platforms. *Journal of Atmospheric and Oceanic Technology*, *35*(2), 281–297.

Yu, X., Ponte, A. L., Elipot, S., Menemenlis, D., Zaron, E. D., & Abernathey, R. (2019). Surface kinetic energy distributions in the global oceans from a high-resolution numerical model and surface drifter observations. *Geophysical Research Letters*, *46*(16), 9757–9766.

Yu, X., Ponte, A. L., Lahaye, N., Caspar-Cohen, Z., & Menemenlis, D. (2021). Geostrophy assessment and momentum balance of the global oceans in a tide-and eddy-resolving model. *Journal of Geophysical Research: Oceans*, *126*(10), e2021JC017422.

Zaron, E. D., & Rocha, C. B. (2018). Internal gravity waves and meso/submesoscale currents in the ocean: anticipating high-resolution observations from the swot swath altimeter mission. *Bulletin of the American Meteorological Society*, *99*(9), ES155–ES157.

Zhao, Z., Wang, J., Menemenlis, D., Fu, L.-L., Chen, S., & Qiu, B. (2019). Decomposition of the multimodal multidirectional m2 internal tide field. *Journal of Atmospheric and Oceanic Technology*, *36*(6), 1157–1173.

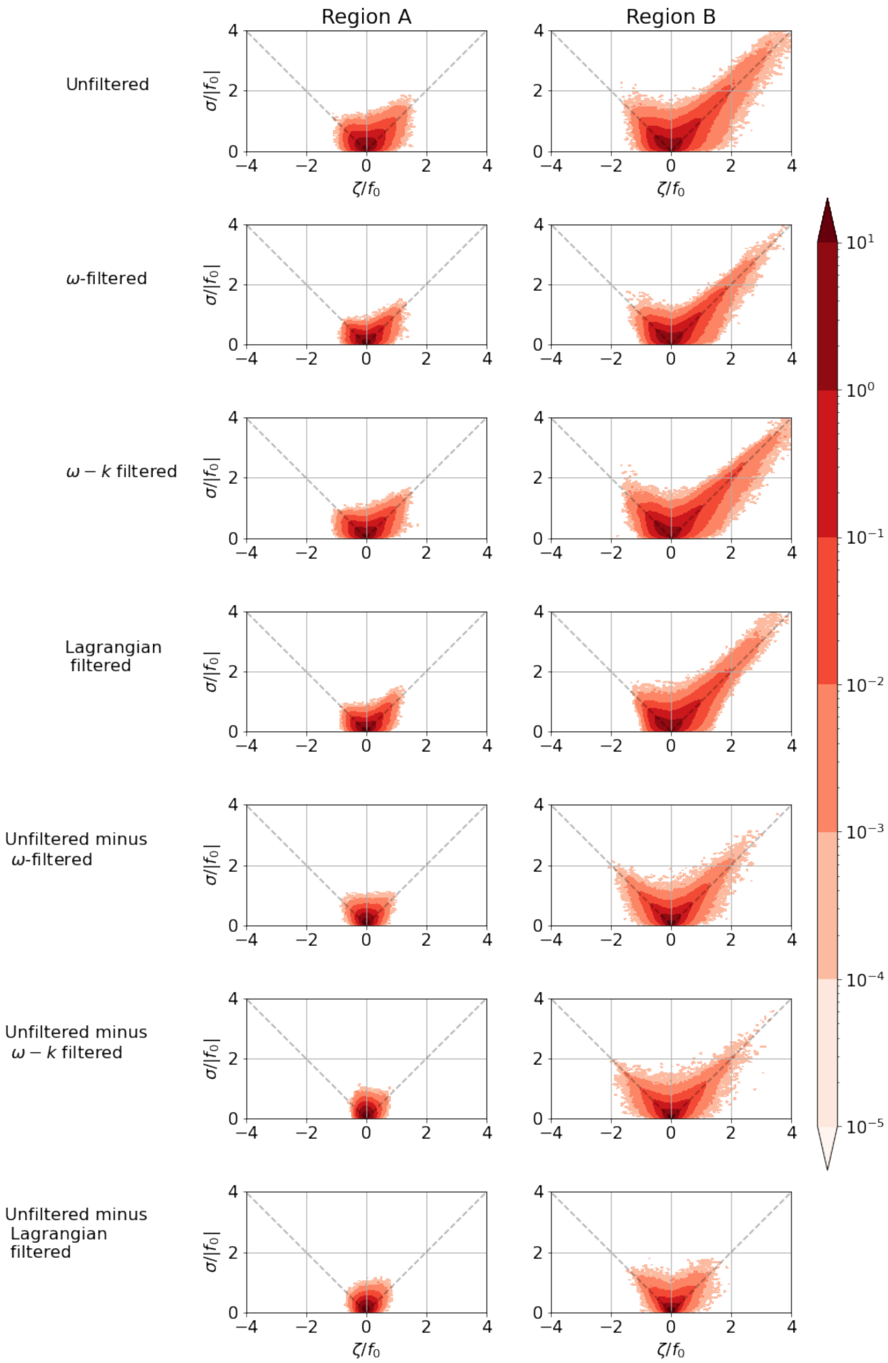

Figure 6. Vorticity-strain joint probability density functions calculated from surface velocities in region A (left) and in region B (right). The dashed lines are the $|\zeta| = \sigma$ lines: submesoscale fronts tend to be concentrated just above the cyclonic $\zeta = \sigma$ line (Balwada et al., 2021). The ω-k filtered velocities are projected onto a tangent plane before the JPDF is calculated, but all other JPDFs are calculated without projection (projection onto a tangent plane introduces a small error in the vorticity and strain fields).

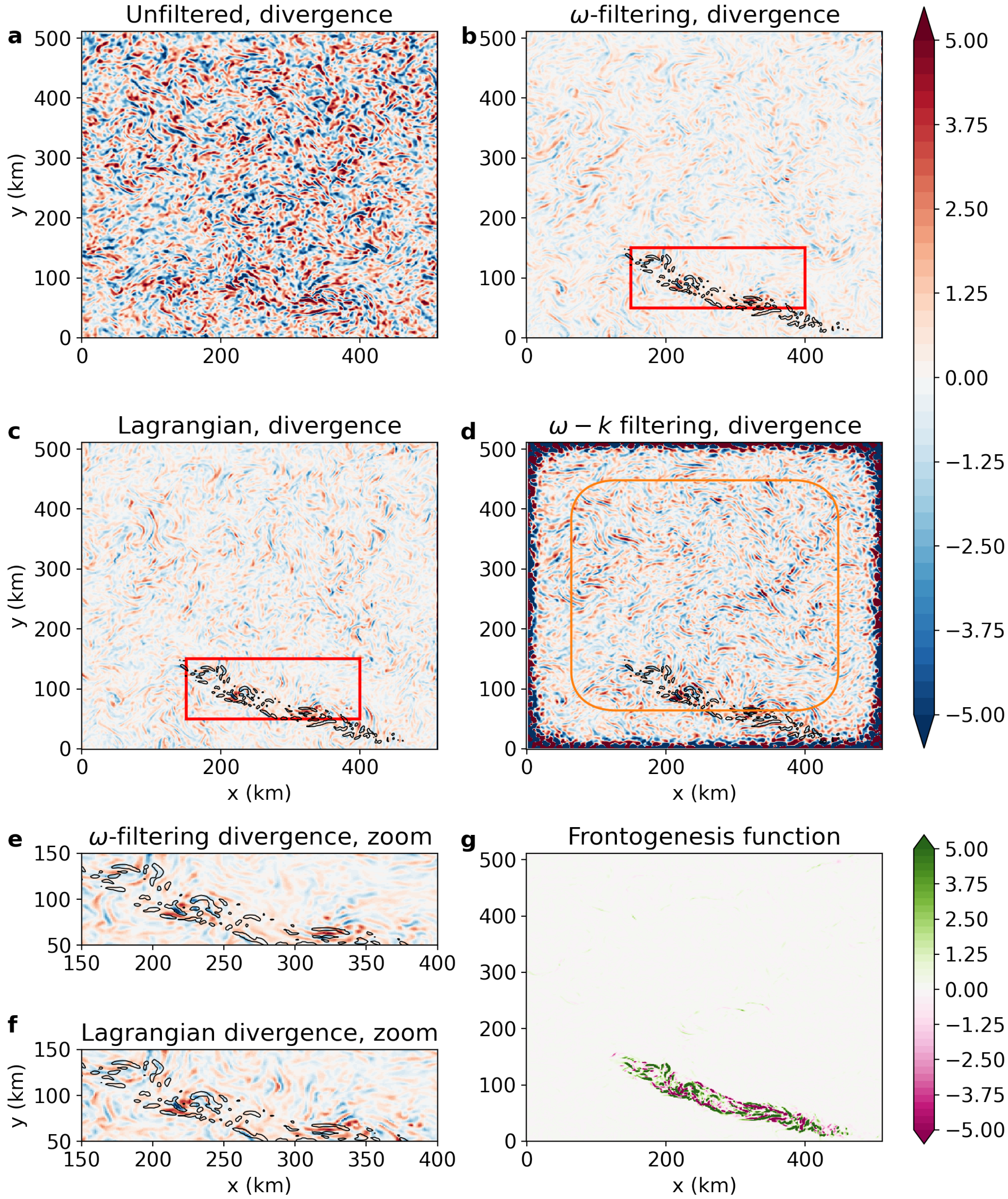

Figure 7. a-d) Divergence ($\times 10^5 \mathrm{s}^{-1}$) of unfiltered and filtered velocities on day 35 in region A, the blue box of figure 1, e-f) the same quantities in the region inside the red box of b) and c) and g) the frontogenesis function ($\times 10^{14} \mathrm{kg}^2/\mathrm{m}^8/\mathrm{s}$). Thin black contours show the 0.2 contour of the frontogenesis function. Inside the orange contour, the window function used in ω-k filtering is greater than 0.5: inside this contour, inaccuracies due to windowing should be negligible.

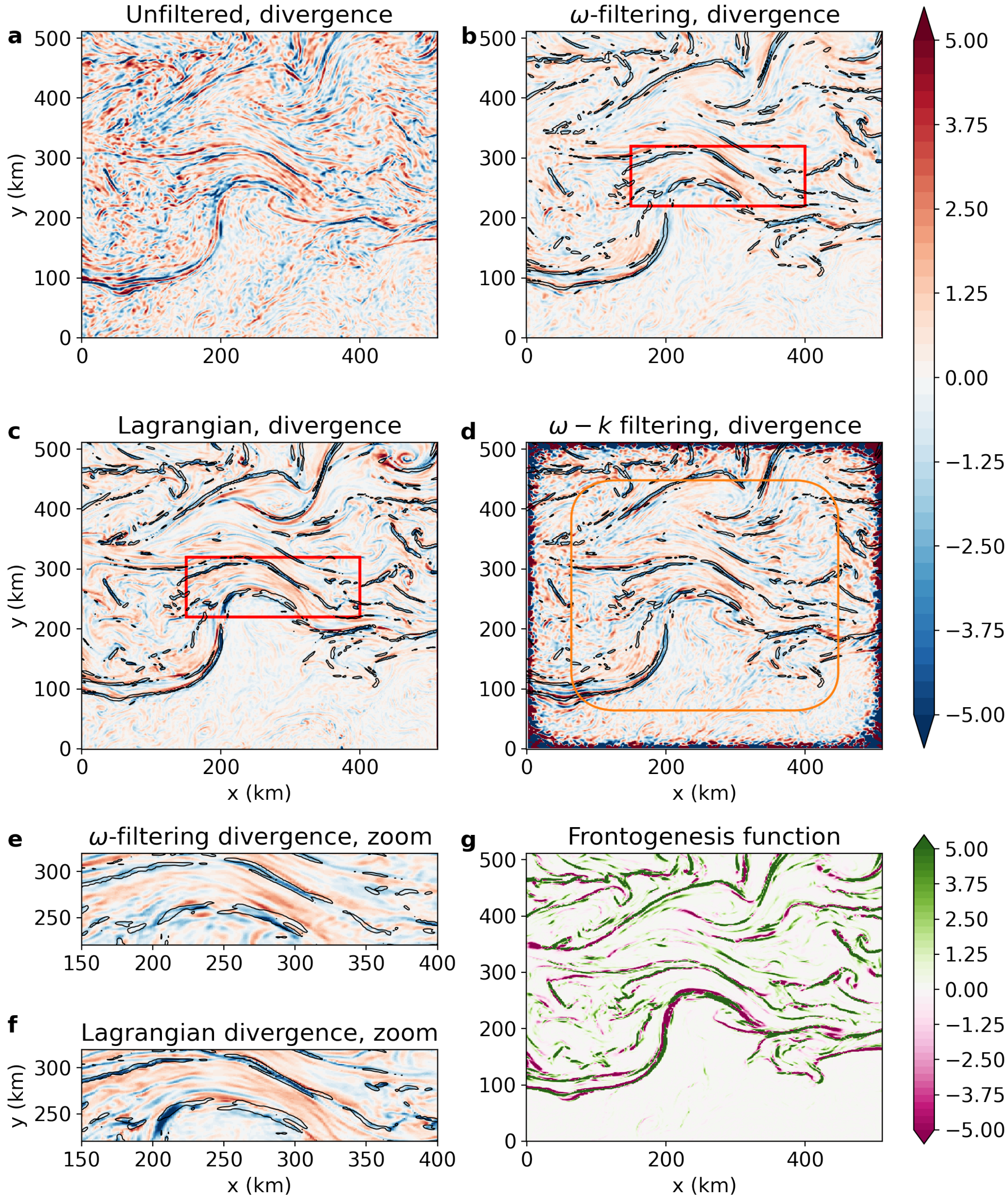

Figure 8. a-d) Divergence ($\times 10^5 \mathrm{s}^{-1}$) of unfiltered and filtered velocities on day 35 inside the green box of figure 1, e-f) the same quantities in the region inside the red box of b) and c) and g) the frontogenesis function ($\times 10^{14} \mathrm{kg}^2/\mathrm{m}^8/\mathrm{s}$). Black contours show the 1 contour of the frontogenesis function. Inside the orange contour, the window function used in ω-k filtering is greater than 0.5: inside this contour, inaccuracies due to windowing should be negligible.

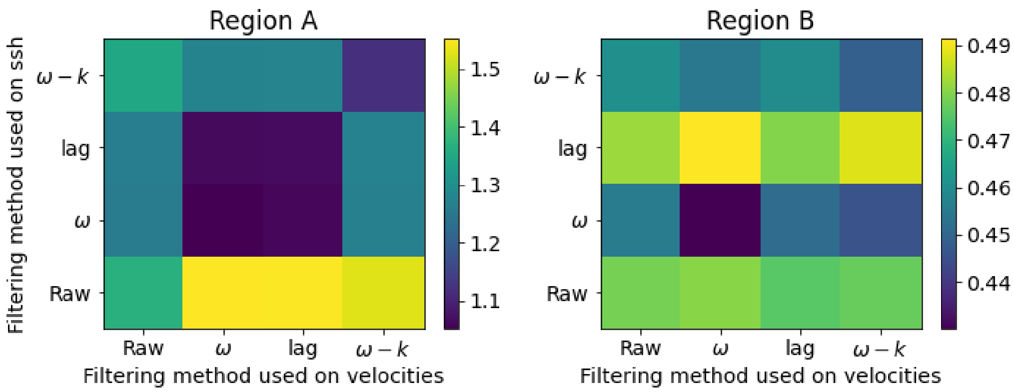

Figure 9. Normalized root mean square difference (RMS^{ij} in equation (9)) between the unfiltered surface speed and the surface speed calculated by applying the geostrophic equation to sea-surface height for the blue box of figure 1 (left) and the green box of figure 1 (right).